RSC Advances

PAPER

Cite this: *RSC Adv.*, 2016, **6**, 61821

Novel RGO–$ZnWO_4$–Fe_3O_4 nanocomposite as high performance visible light photocatalyst†

M. Mohamed Jaffer Sadiq,[a] U. Sandhya Shenoy[b] and D. Krishna Bhat*[a]

A novel RGO–$ZnWO_4$–Fe_3O_4 nanocomposite is synthesized by a microwave irradiation method and its catalytic activity for the photo degradation of Methylene Blue (MB) is investigated. The prepared nanocomposites are characterized by powder X-ray diffraction (XRD), X-ray photoelectron spectroscopy (XPS), high resolution transmission electron microscopy (HRTEM), transmission electron microscopy (TEM), field emission scanning electron microscopy (FESEM), Raman spectroscopy, photoluminescence spectroscopy (PL) and UV-visible spectroscopy. The visible light photocatalytic activities of the prepared nanocomposites are investigated using a MB dye solution. It is noteworthy that RGO–$ZnWO_4$–Fe_3O_4 nanocomposites exhibited relatively high photocatalytic activity compared to $ZnWO_4$–RGO and pure $ZnWO_4$ on MB in aqueous solution. This enhanced rate is due to the ability of the graphene in the RGO–$ZnWO_4$–Fe_3O_4 composite to support carrier exploitation efficiently by tolerating the photo excited electron–hole pairs and thus encouraging oxidative degradation of the pollutants. This work could be extended to other organic pollutants as well and could provide new insights into ternary nanocomposites as high performance photocatalysts and their application in waste water treatment.

Received 19th May 2016
Accepted 16th June 2016

DOI: 10.1039/c6ra13002j

www.rsc.org/advances

Introduction

Toxic organic and inorganic waste from industry are major contaminants of the environment and currently pose a serious problem.[1,2] Photocatalysis is an excellent method for the degradation of highly toxic hazardous pollutants present in waste water.[3,4] Although it is a less expensive process compared to other advanced oxidation processes, the overall cost can be further reduced by optimizing the operating environment. Hence, photocatalysis can be practically implemented in combination with a heterogeneous catalyst and made more cost effective.[5,6] Semiconductor photocatalytic materials are a green tool for the decomposition of organic pollutants into non-hazardous compounds under light irradiation. It is well known that TiO_2 is an excellent photocatalytic material due to its high activity and stability, but it is only active under UV light irradiation because of its wide band gap. Therefore, there is a need to develop novel visible light based photocatalytic materials.

In recent years, graphene based nanocomposites have attracted attention for photocatalytic processes due to their excellent sensitivity, durability and stability.[6] Several research groups are working on graphene-based nanocomposite materials like graphene oxide (GO)–polymer, GO–metal, GO–semiconductor, GO–metal oxide and GO–magnetic material composites for various engineering applications due to its high surface area and high chemical stability.[7] Further, graphene has also been used profusely as an active supporting component in the preparation of nanocomposite materials for adsorption, separation and degradation of organic dyes from industrial waste water.[8,9]

Moreover, to improve the photocatalytic activity of materials, many research groups are focusing on the combination of metal oxides and tungstates to transfer the photoinduced electrons. The combination of graphene and metal tungstates/oxides is believed to increase the photoelectron transfer rate and enhance photocatalytic activity. Several reports are available in which transition metal oxides and carbon based metal oxide nanocomposites are used as a catalyst material for water purification.[10–14] Generally, metal tungstates ($BaWO_4$, $NiWO_4$, Bi_2WO_6, $ZnWO_4$) are an important class of inorganic materials which can be used in many applications in various fields like photoanodes, luminescent materials, gas-sensing, optical fibers, ceramics and photocatalysts.[15–18] There are several methods to synthesize metal tungstates such as sol–gel, hydrothermal synthesis, solid state methods, ultrasonic irradiation, microwave irradiation and co-precipitation.[19–21]

However, there are only a few reports on graphene based ternary nanocomposites with an outstanding photocatalytic performance.[22,23] In view of this, we report herein the synthesis of RGO–$ZnWO_4$–Fe_3O_4 nanocomposites by a microwave

[a]*Department of Chemistry, National Institute of Technology Karnataka Surathkal, Mangalore-575025, India. E-mail: denthajekb@gmail.com; Fax: +91 824 2474033; Tel: +91 824 2473202*

[b]*Jawaharlal Nehru Centre for Advanced Scientific Research, Jakkur, Bangalore-560064, India*

† Electronic supplementary information (ESI) available. See DOI: 10.1039/c6ra13002j

irradiation method and characterization of the as prepared samples by XRD, Raman, FESEM, TEM, HRTEM, XPS, PL and UV-visible spectroscopic techniques. The photocatalytic activities of the prepared nanocomposites have been studied on an MB solution under visible light irradiation. The resulting RGO–$ZnWO_4$–Fe_3O_4 nanocomposites exhibited relatively high photocatalytic activity and stability. Thus, it could be a promising candidate for the eco-friendly photocatalytic treatment of organic pollutants in waste water.

Experimental

Materials and method

All the chemicals were procured from Sigma Aldrich and were used without further purification. All the reactions were carried out with Millipore water.

Synthesis of GO

GO was synthesized using a modified Hummers method.[24] 1.0 g of natural graphite flakes were stirred with 100 mL of conc. H_2SO_4 in an ice bath. The temperature of the reaction mixture was maintained below 20 °C and 6.0 g of $KMnO_4$ was added slowly under continuous stirring. After the addition the reaction mixture was brought to room temperature and stirred for 12 hours. Then 100 mL of water were added and the reaction mixture was maintained at 98 °C for 2 hours and then cooled to room temperature naturally. As the temperature dropped to 75 °C, 50 mL of DI water and 5 mL of H_2O_2 were added. Then the obtained GO solution was centrifuged 5 times with 10% HCl and several times with water. The sample was freeze-dried to obtain GO powder which was dispersed in ethylene glycol by sonication at a concentration of 1 mg mL^{-1} to form a uniform suspension which was used for further processes.

Synthesis of RGO–$ZnWO_4$ and RGO–$ZnWO_4$–Fe_3O_4 nanocomposites

x-RGO–$ZnWO_4$ (x = 1, 2, 3 and 4 wt% GO) nanocomposite was synthesized by a one-step microwave irradiation method. 0.05 M zinc acetate solution (50 mL) was slowly added to the dispersed GO solution obtained from the procedure above. Then 0.05 M sodium tungstate solution (50 mL) was slowly added to the mixture under constant stirring for about 2 hours. Using ammonia, the pH of the solution was maintained at 9. Later, the mixture was treated with microwave irradiation at 350 W for 10 minutes and was allowed to cool down to room temperature naturally. The blackish precipitate obtained was centrifuged with water and 10% ethanol 5 times. Finally, the obtained powder was dried in a vacuum oven at about 80 °C for 12 hours.

RGO–$ZnWO_4$–Fe_3O_4(y) (y = 0.005, 0.01 and 0.02 M of precursor solution) nanocomposites were also synthesized by the one-step microwave irradiation method. In a typical experiment, to an optimized amount of RGO–$ZnWO_4$ nanocomposite solution, 50 mL of (0.005, 0.01 or 0.02 M as the case is) iron acetate in ethanol and water mixture was added. To this 10 mL of ammonia was added and the reaction mixture was stirred for about 30 minutes before subjecting it to 350 W microwave radiation for 10 minutes. The obtained precipitate was washed with water and ethanol and dried in vacuum oven at 80 °C for 12 hours. The same procedure was repeated for the sake of comparison without the use of GO.

Characterization

The structural characterization of the synthesized nanocomposites was performed using an X-ray diffractometer (Rigaku, Japan) using nickel filtered Cu K_α radiation at a scan rate of 1° per minute in the range of 5–70°. The surface morphology was observed using SEM, (JEOL), FESEM, (Zeiss Ultra 55), TEM (Tecnai G20), high resolution transmission electron microscope (HRTEM, Tecnai). Raman spectra were measured by a laser Raman microscope (Renishaw Invia) with a 532 nm excitation laser from a He–Ne source. The surface elemental analysis of the as-synthesized samples was performed by X-ray photoelectron spectroscopy (XPS, Multilab 2000 Thermo scientific, UK) using Mg K_α X-rays with 200 W power as excitation source and 10 eV energy pass for data collection. The room temperature photoluminescence spectrum was measured with a 380 nm excitation wavelength source (LS-55, Perkin Elmer Instruments). The absorbance spectra were taken from a UV-visible spectrophotometer (Analytik Jena).

Determination of photocatalytic activity

Determination of the photocatalytic activity of MB dye was carried out using a photoreactor under ambient atmospheric conditions. The photoreactor was equipped with a 250 W Hg lamp fitted with a 400 nm cut-off filter, as a source of visible light irradiation. In these experiments, 200 mL of MB dye solution (10 mg L^{-1}) and photocatalyst (20 mg) were added into a 500 mL of Pyrex glass beaker and stirred for about 30 minutes in the dark to reach the adsorption–desorption equilibrium of the photocatalyst. Then the solution was exposed to visible light irradiation. During photocatalytic studies, at regular time intervals, 4 mL of the reacted MB solution was taken out, centrifuged and the supernatant solution was used to measure the concentration of the MB solution through UV-visible spectroscopic analysis at a wavelength of 664 nm. The percentage of degradation of dye was calculated as per eqn (1).[25]

$$\text{Percentage of degradation of dye} = ((C_A - C_B)/C_A) \times 100 \quad (1)$$

where, C_A is the initial absorbance and C_B is the absorbance at a given interval time of the MB dye solution, respectively. Further, all the data presented are averages of three independent measurements.

Results and discussion

XRD studies

Fig. 1 shows the XRD patterns of the as-prepared RGO, $ZnWO_4$, Fe_3O_4 and RGO–$ZnWO_4$–Fe_3O_4. The diffraction peaks at 22.6° and 42.6° were ascribed to (002) and (100) planes of RGO sheets. The diffraction peaks at 15.3°, 18.7°, 23.6°, 24.3°, 30.4°, 36.3°,

38.2°, 41.0°, 44.4°, 45.5°, 48.6°, 50.1°, 51.5°, 53.9°, 61.7°, 64.9° and 68.1° were ascribed to the (010), (100), (011), (110), (111), (021), (200), (121), (112), (211), (022), (220), (130), (122), (113), (311) and (041) crystal planes of $ZnWO_4$ and conform well to JCPDS file no. 15-0774. Similarly, the diffraction peaks at 30.3°, 35.6°, 43.4°, 53.7°, 57.3° and 62.9° can be indexed to the (220), (311), (400), (422), (511) and (440) crystal planes of Fe_3O_4 and are in good agreement with JCPDS file no. 19-0629. No obvious carbon diffraction peak for RGO was detected in the XRD patterns of the RGO–$ZnWO_4$–Fe_3O_4 nanocomposite, which may be due to the small amount of RGO in the composite samples.[26] Further, crystal sizes were deduced from the highest intensity peaks of XRD patterns corresponding to (111) and (311) planes of $ZnWO_4$ and Fe_3O_4 respectively. The average crystal sizes were calculated from the Scherrer equation[27] to be around 17 nm and 13.3 nm for $ZnWO_4$ and Fe_3O_4 in the RGO–$ZnWO_4$–Fe_3O_4 composite respectively. Thus these results suggest that $ZnWO_4$ and Fe_3O_4 particles were decorated on RGO nanosheets. The existence of RGO in the composites was confirmed by Raman, FESEM and TEM analysis.

Raman studies

The obtained Raman spectra of as-prepared RGO–$ZnWO_4$–Fe_3O_4 composite samples are shown in Fig. 2. As can be observed from the figure, two peaks at 1347.7 cm^{-1} and 1601.1 cm^{-1} correspond to the characteristic Raman mode of the plane vibrations of sp^3 defects in carbon (D band) and sp^2 bonded carbons (G band) of the RGO sheets. the above mentioned results confirmed that the RGO–$ZnWO_4$–Fe_3O_4 nanocomposites are successfully anchored to the RGO sheets and such results are also available in the literature.[28] Further, the D to G band peak intensity ratio, I_D/I_G is generally used to confirm the degree of defects of the carbon nanomaterial. As shown in Fig. 2, the calculated intensity ratio of RGO and RGO–$ZnWO_4$–Fe_3O_4 (I_D/I_G = 1.10 and 1.03) is higher than that of GO (I_D/I_G = 0.98),

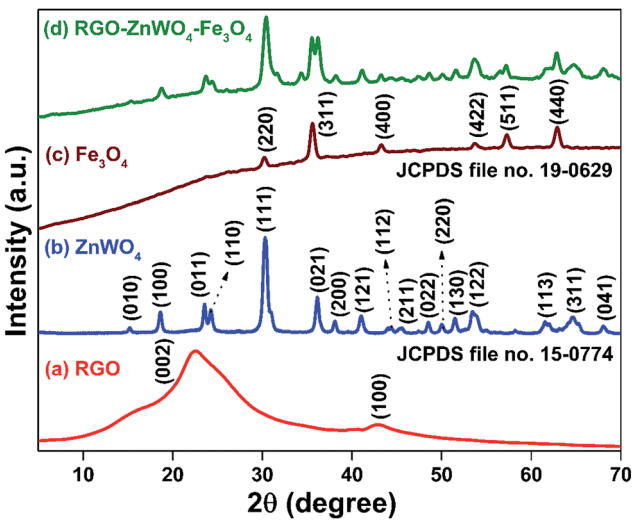

Fig. 1 XRD spectrum of (a) RGO, (b) $ZnWO_4$, (c) RGO–$ZnWO_4$ and (d) RGO–$ZnWO_4$–Fe_3O_4.

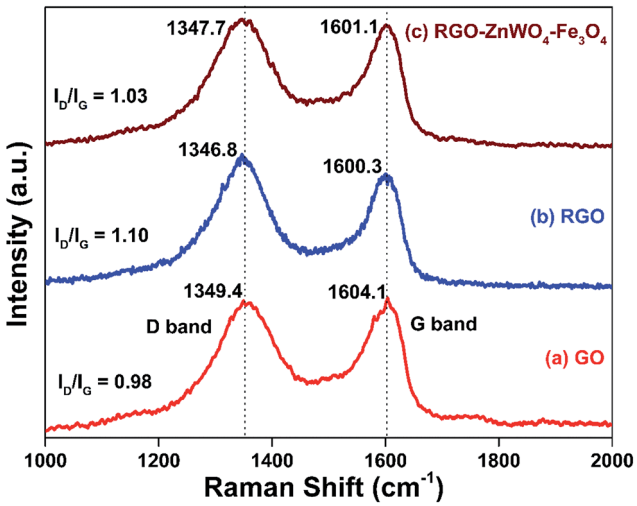

Fig. 2 Raman spectra of GO, RGO, RGO–$ZnWO_4$–Fe_3O_4.

indicating the introduction of defects during the reduction of GO into RGO sheets. The lower I_D/I_G of RGO–$ZnWO_4$–Fe_3O_4 than that of RGO may be due to the adherence and interaction of $ZnWO_4$ and Fe_3O_4 nanoparticles on the RGO sheets. Moreover, the broad D band and G band with weak intensity may be ascribed to the low content of RGO and relatively higher concentration and interaction of $ZnWO_4$ and Fe_3O_4 nanoparticles on the RGO sheets.[29]

Morphology studies

The structure and morphological features of synthesized RGO–$ZnWO_4$–Fe_3O_4 nanocomposite materials were investigated by microscopic techniques. Fig. 3a shows the SEM image of the RGO with a crumpled sheet like structure. Rod like shapes of $ZnWO_4$ can be identified from Fig. 3b. Fig. 3c shows the SEM image of the Fe_3O_4 particles with spherical like structure. Fig. 3d shows the SEM image of the RGO–$ZnWO_4$–Fe_3O_4 nanocomposite wherein $ZnWO_4$ nanorods and Fe_3O_4 nanospheres are anchored on the surface of the RGO nanosheets.

To get further information on the morphology of the synthesized materials, TEM and HRTEM were carried out. Fig. 4a shows the TEM image indicating the two dimensional wrinkled sheet like morphology of RGO. The TEM image of the synthesized $ZnWO_4$ is shown in Fig. 4b, which clearly reveals the nanorod-like structures. As can be observed from Fig. 4c, the rod-like $ZnWO_4$ and spherical Fe_3O_4 nanoparticles adhere to the surface of the RGO nanosheets. Fig. 4d shows the HRTEM image of RGO–$ZnWO_4$–Fe_3O_4 wherein, the interface between $ZnWO_4$ and Fe_3O_4 nanomaterials on the surface of the RGO nanosheets can be seen. The lattice fringes of about 0.367 nm correspond to the (011) plane of $ZnWO_4$ and 0.258 nm corresponds to the (311) plane of Fe_3O_4. Thus, it is evident that the interface is formed by the Fe_3O_4 (311) plane and the $ZnWO_4$ (011) plane on the surface of the RGO sheets. The SAED pattern (inset of Fig. 4d) further shows that $ZnWO_4$ and Fe_3O_4 nanoparticles on the RGO sheets are of polycrystalline nature.

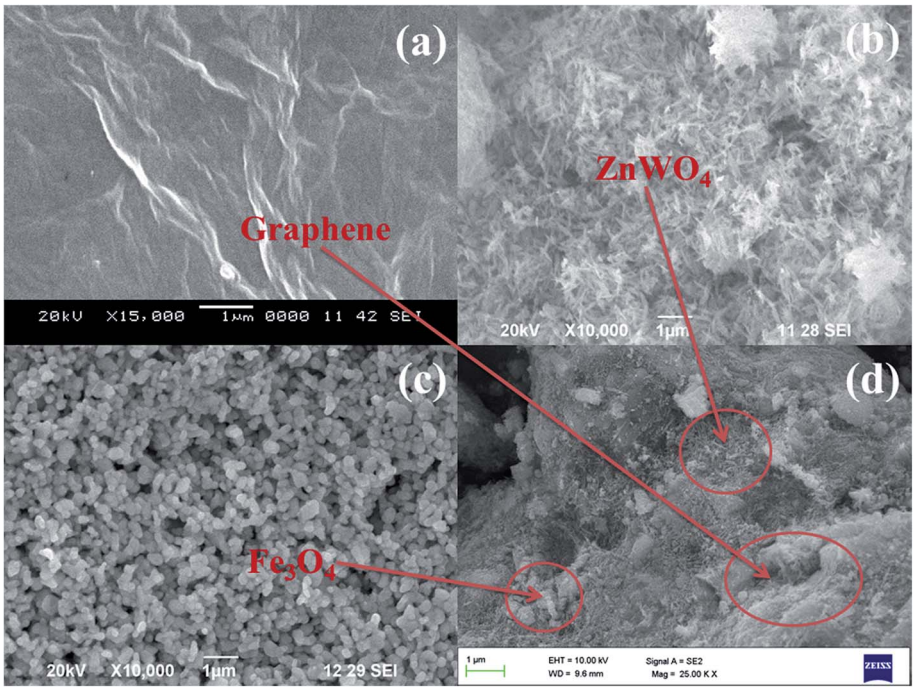

Fig. 3 Scanning electron microscopy images of (a) RGO (b) $ZnWO_4$ and (c) Fe_3O_4. Field emission scanning electron microscopy image of (d) RGO–$ZnWO_4$–Fe_3O_4.

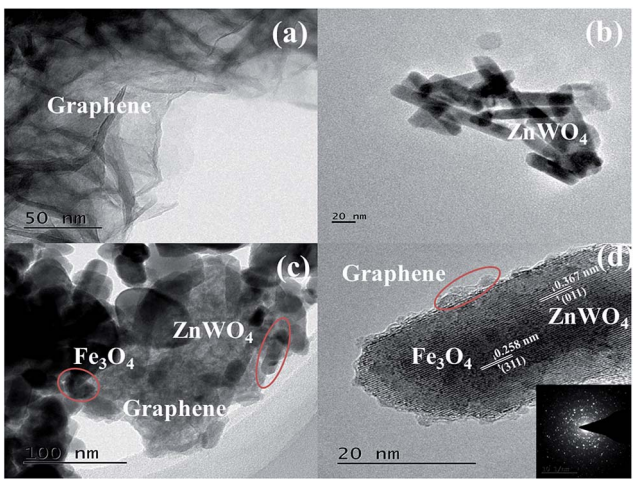

Fig. 4 Transmission electron microscopy images of (a) RGO (b) $ZnWO_4$ (c) RGO–$ZnWO_4$–Fe_3O_4 (d) high resolution transmission electron microscopy image of RGO–$ZnWO_4$–Fe_3O_4; inset: SAED.

XPS studies

Fig. 5 shows detailed information on the chemical states of ions present in the as-prepared samples through XPS analysis. According to XPS analysis, binding energy was calibrated by using the C 1s peak (284.8 eV) as a reference. Fig. 5a shows the general survey XPS spectra of the as-prepared RGO–$ZnWO_4$–Fe_3O_4 nanocomposites the surface of which contains C, Zn, W and Fe. Fig. 5b shows the high resolution C 1s spectra which could be deconvoluted into four peaks of different binding energies, 284.8 eV, 286.6 eV, 288.1 eV and 290.1 eV. These peaks correspond to the C–C/C=C in the aromatic ring of sp^2, C–O, C=O and O–C=O bonds in the oxygenated functional groups respectively. The intensity of the oxygen bonded group peaks are much smaller compared to that of the C–C/C=C peak. These peaks will have comparable intensity in the GO in general. Hence these results indicate that the oxygen functional groups have been considerably reduced to form RGO sheets.[30] Fig. 5c shows the high resolution O 1s spectra which could be deconvoluted into two peaks of binding energy values, 529.9 eV and 531.6 eV corresponding to Fe–O and W–O–W bonds respectively.[31] Fig. 5d shows the high resolution Zn 2p region, with two broad peaks at 1019.1 eV and 1041.9 eV which are indexed to Zn $2p_{3/2}$ and Zn $2p_{1/2}$ state, respectively.[32] Fig. 5e shows the high resolution W 4f spectra which could be deconvoluted into two different peaks at 36.8 eV and 38.8 eV being allotted to W $4f_{7/2}$ and W $4f_{5/2}$, respectively. These results are also in conformity with that of the $ZnWO_4$ values reported previously.[32] Fig. 5f shows the high resolution Fe 2p region with two photoelectron peaks at 709.2 eV and 723.5 eV. They correspond to Fe $2p_{3/2}$ and Fe $2p_{1/2}$, states of iron respectively. These results ascertain that a composite of Fe_3O_4, $ZnWO_4$ and graphene sheets has been formed successfully[33–35] and the same has also been supported by the HRTEM studies (Fig. 4c and d).

Optical absorbance analysis

Fig. 6 shows the absorption spectrum of RGO–$ZnWO_4$–Fe_3O_4, RGO–$ZnWO_4$, pure $ZnWO_4$ and pure Fe_3O_4. The band gap is the most important factor with regard to the photocatalytic activity of the materials. To calculate the band gap of the materials, the Tauc relation as given in eqn (2) was used[25]

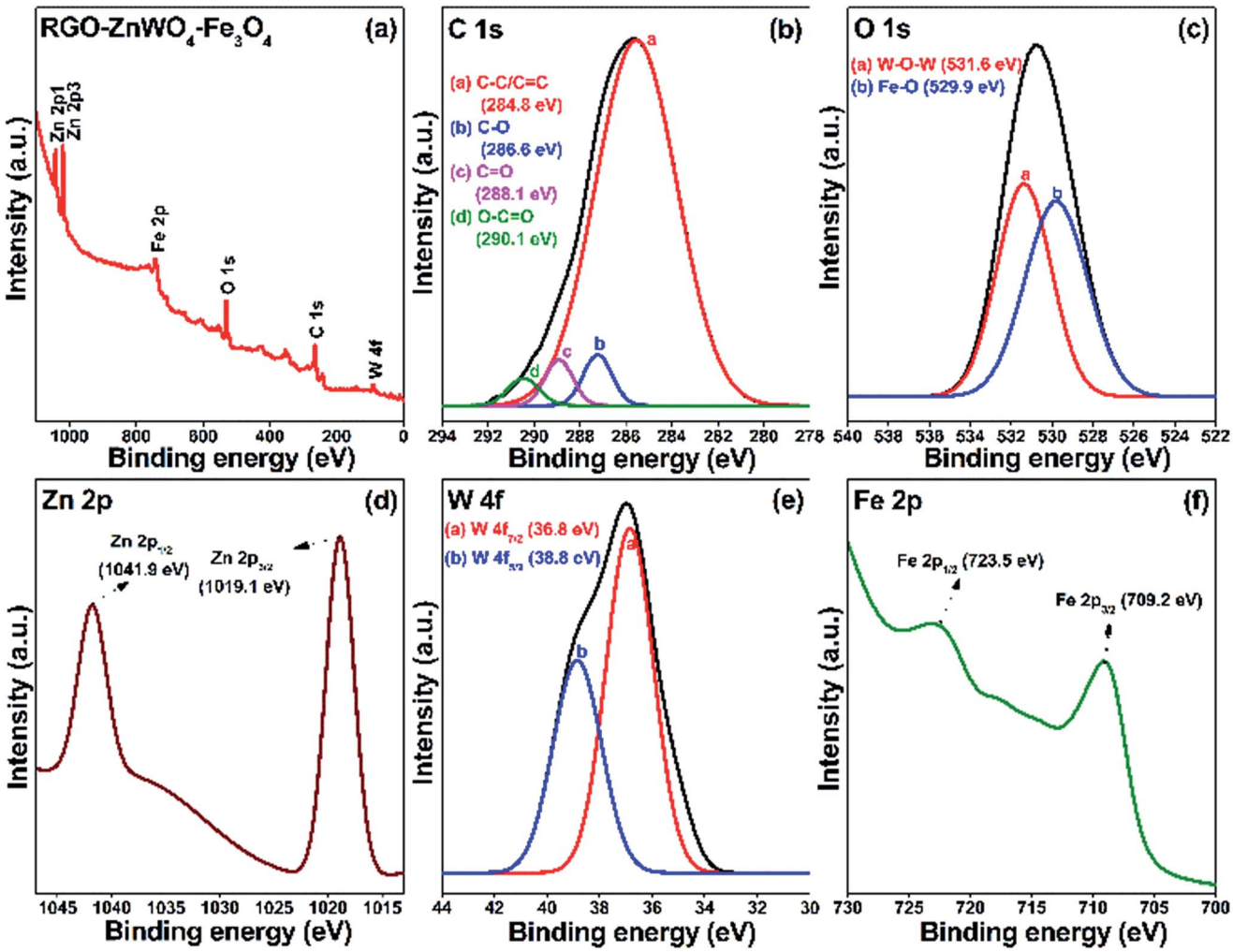

Fig. 5 XPS spectra of as-prepared samples (a) survey of RGO–$ZnWO_4$–Fe_3O_4. High-resolution XPS spectra of (b) C 1s, (c) O 1s, (d) Zn 2p, (e) W 4f and (f) Fe 2p.

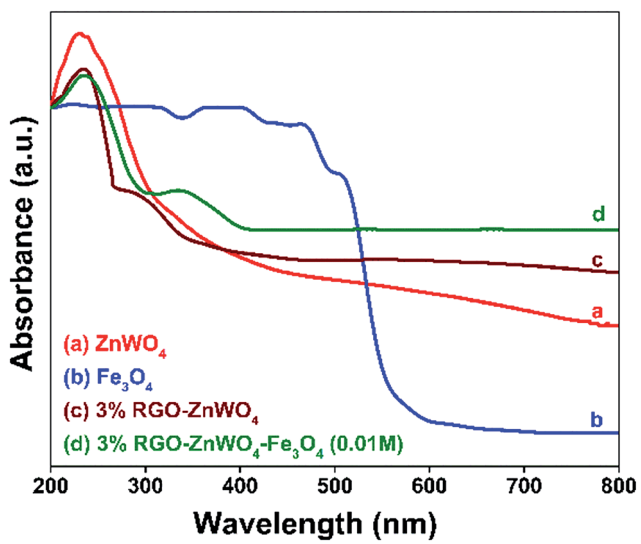

Fig. 6 UV-vis spectra of (a) $ZnWO_4$, (b) Fe_3O_4, (c) RGO–$ZnWO_4$ and (d) RGO–$ZnWO_4$–Fe_3O_4.

$$\alpha h\nu = K(h\nu - E_g)^{n/2} \quad (2)$$

where α is the absorption coefficient, $h\nu$ is the energy of a photon, K is a constant, E_g is the band gap of the semiconductor. Among these parameters, n is determined by the type of transition process that occurs in a semiconductor ($n = 1$ for a direct transition and $n = 4$ for an indirect transition). The direct band gap is considered in general for semiconductor photocatalysis processes.[34–36] Accordingly, the band gap energies (E_g) for pure $ZnWO_4$, RGO–$ZnWO_4$, Fe_3O_4 and RGO–$ZnWO_4$–Fe_3O_4 nanocomposites were estimated from a plot of $(\alpha h\nu)^2$ *versus* energy ($h\nu$), as shown in ESI (ESI; S1 and S2†). As can be seen from the figure, a strong absorption edge at 313 nm is observed for pure $ZnWO_4$ which is equivalent to a band gap of 3.35 eV. The same for the RGO–$ZnWO_4$ nanocomposite is estimated to be at 353 nm which is equivalent to a band gap of 3.0 eV. Similarly, the calculated band gap for the ternary RGO–$ZnWO_4$–Fe_3O_4 nanocomposite is 2.71 eV. The band gap narrowed from 3.35 to 2.71 eV for the RGO–$ZnWO_4$–Fe_3O_4 nanocomposite, indicating the interaction between these three components. It is therefore evident that the RGO–$ZnWO_4$–Fe_3O_4

nanocomposite facilitates strong absorption in the visible region of the spectrum and the phenomena can be attributed to the synergetic effects of $ZnWO_4$, Fe_3O_4 and RGO nanosheets.[37,38] The results clearly suggest that the novel ternary composite can perform efficiently as a photocatalyst under visible light.

Photoluminescence analysis

It is well known that a PL spectrum is a very useful tool to study the dynamics of separation and recombination of photogenerated electron–hole pairs. This is mainly due to the fact that the PL emission signal arises from the recombination of excited electrons and holes. It is also well established that the electron–hole pair separation improves the photocatalytic performance of materials. The photo induced electron hole pair transfer mechanism in the RGO sheets, $ZnWO_4$ and Fe_3O_4 nanomaterials are determined by the photoluminescence emission intensity. The PL spectra of RGO–$ZnWO_4$–Fe_3O_4, RGO–$ZnWO_4$ and pure $ZnWO_4$ nanocomposites are measured using an excitation wavelength of about 380 nm (Fig. 7). The PL spectrum of $ZnWO_4$ shows a high intensity broad peak at 441 nm which corresponds to the recombination of photogenerated electron hole pairs. The weak intensity of the RGO–$ZnWO_4$ nanocomposite may be due to the transfer of photoinduced electrons from the trapped states of $ZnWO_4$ to the RGO nanosheets.[39] As can be seen from the figure, the PL intensity of the RGO–$ZnWO_4$–Fe_3O_4 nanocomposite is very weak indicating that the fluorescence of this nanocomposite is quenched in a more powerful manner than that of RGO–$ZnWO_4$ nanocomposite proving the synergistic effect induced by zinc tungstate and iron oxide component *via* the RGO interlayer in the nanocomposite towards the separation of electron hole pairs and in turn facilitating the energy absorption. This observation suggests that the combination of $ZnWO_4$ and Fe_3O_4 on RGO nanosheets can enhance the prevention of the photoinduced electron hole pair recombination.[40]

Photocatalytic activity

The photocatalytic activity of the as-prepared materials was estimated for the degradation of MB solution under visible light irradiation. The adsorption of the MB solution was carried out for 30 minutes in the dark to reach the adsorption–desorption equilibrium of the photocatalysts before exposing it to the visible light. In a blank test wherein the MB solution was taken without any photocatalyst in the reactor, there was no appreciable degradation. This result suggests that the photolysis is negligible. The RGO composition in the RGO–$ZnWO_4$ nanocomposites was optimized based on the degradation of MB results. Fig. 8 shows the photocatalytic degradation of RGO–$ZnWO_4$ nanocomposites with varying amounts of RGO. It is observed that the photocatalytic degradation efficiency of the nanocomposites increased with increase in RGO content up to 3% which registered 85% conversion within 150 minutes whereas the same for pure $ZnWO_4$ under the same conditions was only 60%. However a further increase in the RGO content decreased the efficiency of the nanocomposite and this behavior may be due to the fact that the superfluous RGO hinders the photon absorption by the semiconductor and hence in turn reduces the efficiency. As 3 wt% RGO–$ZnWO_4$ nanocomposite showed the best activity, the same was taken as the optimized base material for further variation in the Fe_3O_4 content.

Fig. 9 shows the photocatalytic degradation of MB by 3 wt% RGO–$ZnWO_4$ with 0.005, 0.01 and 0.02 M Fe_3O_4 nanosphere content. The photocatalytic activity of the nanocomposites increased with the increase in Fe_3O_4 content. The nanocomposite with 0.01 M Fe_3O_4 content showed maximum efficiency and degraded the dye almost completely within 135 minutes. This result confirms that the ternary 3 wt% RGO–$ZnWO_4$–Fe_3O_4 (0.01 M) nanocomposite is very efficient as a photocatalyst under visible light irradiation.

The kinetics of photocatalytic degradation of MB dye by the prepared nanocomposites conforming to the pseudo first-order rate equation as given in eqn (3) are shown in Fig. 10.

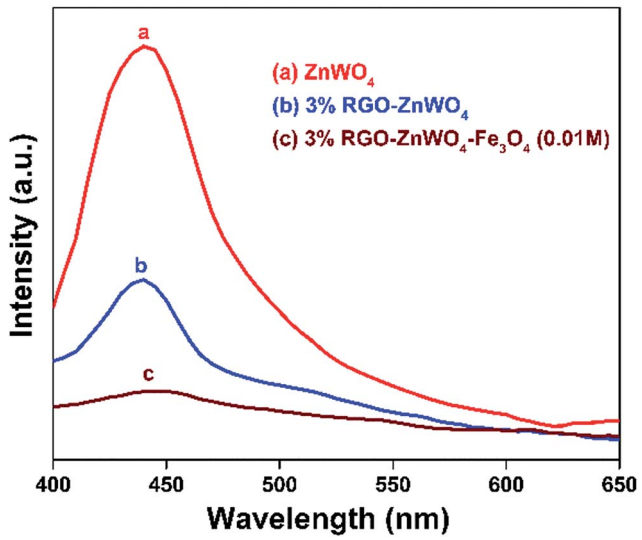

Fig. 7 PL spectra of (a) $ZnWO_4$, (b) RGO–$ZnWO_4$ and (c) RGO–$ZnWO_4$–Fe_3O_4.

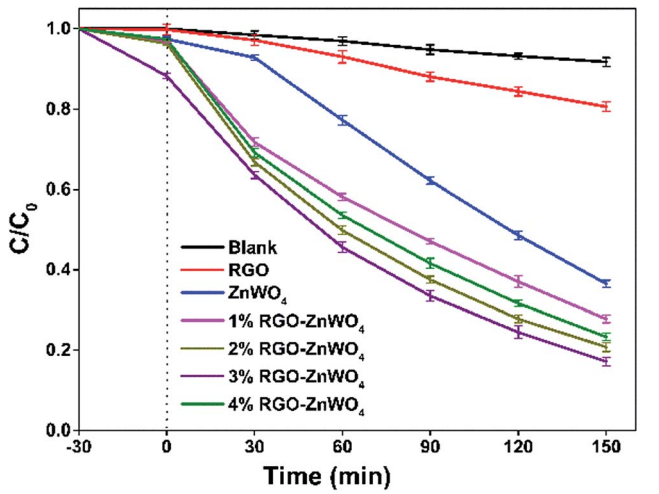

Fig. 8 Degradation rates for MB by RGO–$ZnWO_4$ under visible light irradiation.

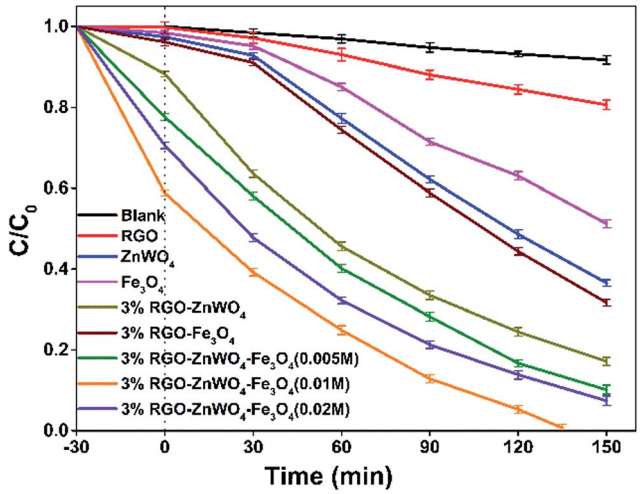

Fig. 9 Degradation rates for MB by RGO–$ZnWO_4$–Fe_3O_4 under visible light irradiation.

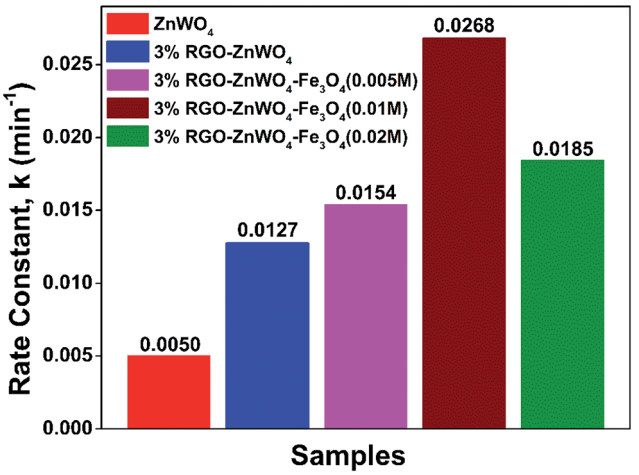

Fig. 11 Degradation rate constant k (min^{-1}) for the photodegradation of MB by RGO–$ZnWO_4$–Fe_3O_4 under visible light irradiation.

$$\ln(C_B/C_A) = -kt \quad (3)$$

where, C_A is the initial concentration, C_B is the concentration at irradiation time (t) and k is the first order rate constant. The k values were measured from the slope of the straight line. A comparison of the rate constants for different nanocomposites is shown in a bar diagram, Fig. 11. As can be seen from the diagram, the best composite shows five times and two times more efficiency than the pure $ZnWO_4$ and 3% RGO–$ZnWO_4$ respectively. However, a further increase in Fe_3O_4 nanoparticle content in the nanocomposite decreased the photocatalytic degradation rate of MB dye which is ascribed to the hindrance of the cluster of Fe_3O_4 nanoparticles present on the ternary nanocomposites to effective charge transfer on RGO sheets. The reusability of ternary nanocomposites is of great need for practical applications. To evaluate the reusability of the 3 wt% RGO–$ZnWO_4$–Fe_3O_4 (0.01 M) nanocomposite, the photocatalytic activity of MB under visible light irradiation was tested for 5 consecutive cycles and the same is shown in Fig. 12. It is observed that there is only minimum loss of photocatalytic degradation efficiency during the test and the MB dye was almost completely degraded within 150 minutes even in the 5th cycle. This indicates that the 3 wt% RGO–$ZnWO_4$–Fe_3O_4 (0.01 M) composite possesses sufficient stability for photocatalytic degradation reactions and that the novel RGO–$ZnWO_4$–Fe_3O_4 nanocomposite can be used as an environmentally friendly photocatalyst for water treatment.

Mechanism of the photocatalytic activity

The enhanced photocatalytic activity of RGO–$ZnWO_4$–Fe_3O_4 composites is mainly related to the superior photo absorption in the visible region and the efficient generation, separation and transfer of the photoinduced electron–hole pairs, which

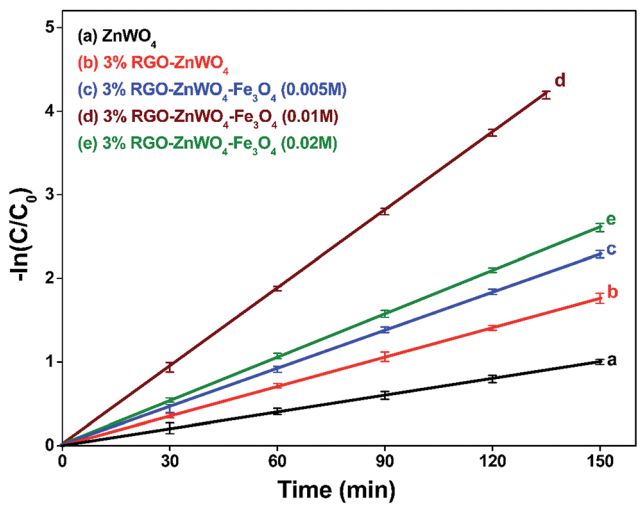

Fig. 10 First order kinetics plot for the photodegradation of MB by RGO–$ZnWO_4$–Fe_3O_4 under visible light irradiation.

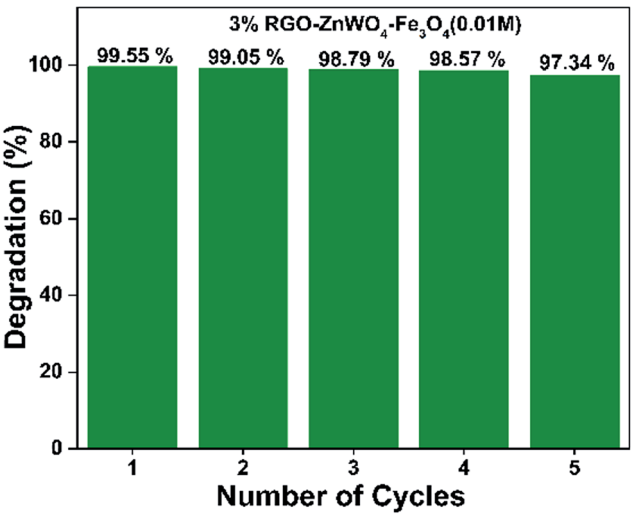

Fig. 12 Recyclability of 3% RGO–$ZnWO_4$–Fe_3O_4 (0.01 M) catalyst for the photodegradation of MB under visible irradiation.

strongly depends on the overall band structure of the composites. Thus, the valence band (VB) edge positions and the conduction band (CB) edge positions of the $ZnWO_4$ and Fe_3O_4 were estimated according to the Mulliken electronegativity theory[32,41] following eqn (4) & (5).

$$E_{VB} = \chi - E^e + 0.5E_g \quad (4)$$

$$E_{CB} = E_{VB} - E_g \quad (5)$$

where E_{VB} is the VB edge potential, E_{CB} is the CB edge potential, E_g is the band gap energy of the semiconductor, χ is the electronegativity of the semiconductor that is the geometric mean of the electronegativity of the constituent atoms and E^e is the energy of free electrons on the hydrogen scale (−4.5 eV). According to the χ and E_g values, E_{VB} and E_{CB} of $ZnWO_4$ and Fe_3O_4 were separately calculated as listed in Table 1.

On the basis of the above results, a photodegradation mechanism for the highly efficient electron–hole pair charge separation of the RGO–$ZnWO_4$–Fe_3O_4 nanocomposites is proposed as shown in Fig. 13. Clearly, Fe_3O_4 can be easily excited to form electron–hole pairs under visible light irradiation. In the case of $ZnWO_4$, excitation by visible light irradiation is not possible due to its wide energy gap. When Fe_3O_4 is introduced, the electrons in CB edge of Fe_3O_4 would easily get transferred to the CB of $ZnWO_4$ *via* the RGO interlayer, leaving holes at the VB of Fe_3O_4. Thus, the photoinduced electrons and holes can be efficiently separated overturning the possibility of the recombination of electron–hole pairs. The separated holes will directly react with MB or react with water to generate hydroxyl radicals. The separated electrons would subsequently react with water and oxygen to generate hydroxyl and superoxide radicals. The radicals would subsequently oxidize the MB due to their high oxidative capacity to harmless degraded products.

The improvement in the photocatalytic performance of the RGO–$ZnWO_4$–Fe_3O_4 nanocomposites is mainly due to the high efficiency in the separation of the photogenerated charge facilitated by the combination of $ZnWO_4$ and Fe_3O_4 *via* the RGO interlayer.

Table 1 Band gap parameters of $ZnWO_4$ and Fe_3O_4

Sample	χ (eV)	E_g (eV)	E_{VB} (eV)	E_{CB} (eV)
$ZnWO_4$	6.313	3.35	3.488	0.138
Fe_3O_4	5.783	2.61	2.588	−0.022

Conclusions

In summary, a simple microwave irradiation method for the synthesis of novel noble metal free ternary RGO–$ZnWO_4$–Fe_3O_4 nanocomposites is reported. The structural, surface morphological and optical properties of the as-synthesized RGO–$ZnWO_4$–Fe_3O_4 nanocomposites were studied by XRD, Raman, SEM, FESEM, TEM, HRTEM, XPS, PL and UV-visible

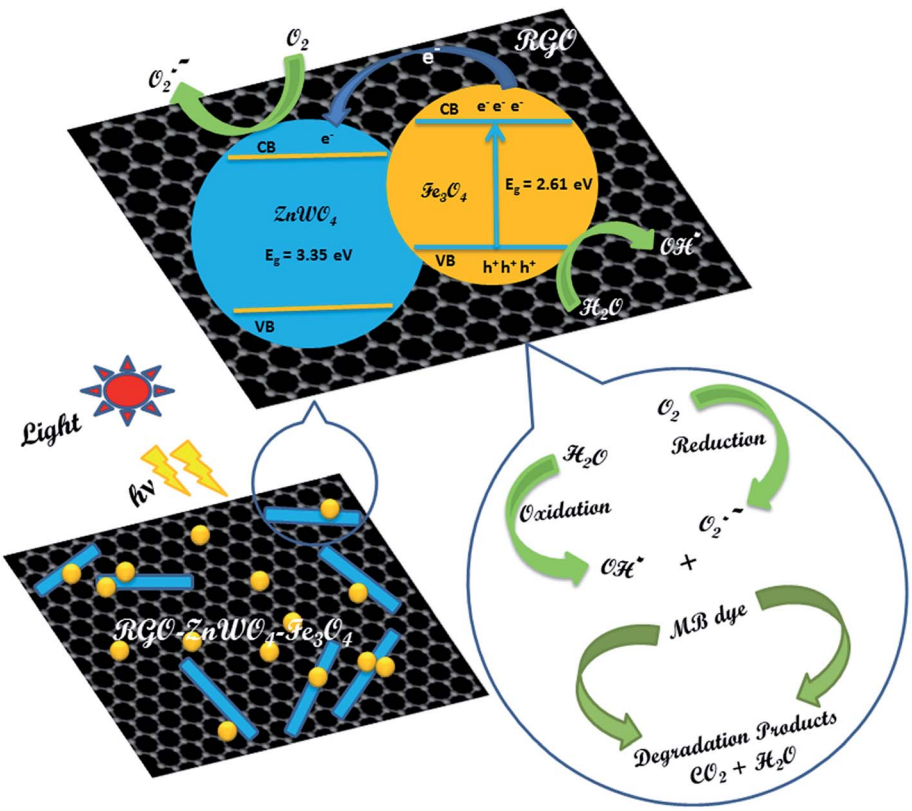

Fig. 13 Schematic diagram of MB photodegradation over RGO–$ZnWO_4$–Fe_3O_4 nanocomposites under visible light irradiation.

spectroscopic techniques. The visible light photocatalytic activities of the as-prepared nanocomposites were evaluated using MB solution. It is seen that 3 wt% RGO–$ZnWO_4$–Fe_3O_4 (0.01 M) is the optimum concentration for efficient catalysis of MB decomposition. It is shown that the synergistic effects of the components of the catalyst are responsible for the enhanced photocatalytic activity. The nanocomposites showed high activity and high stability, even after 5 cycles of photocatalytic processes. The observed results confirmed that RGO–$ZnWO_4$–Fe_3O_4 nanocomposites provide new insights towards novel ternary nanocomposites and can be a potential candidate for the environmental eco-friendly photocatalytic treatment of organic pollutants in water.

Acknowledgements

M. M. J. S. is grateful to the National Institute of Technology Karnataka Surathkal, Mangalore, for providing financial support in the form of Institute fellowship along with essential facilities to carry out this research work.

Notes and references

1 N. Patel, R. Jaiswal, T. Warang, G. Scarduelli, A. Dashora, B. Ahuja, D. Kothari and A. Miotello, *Appl. Catal., B*, 2014, **150**, 74–81.
2 W. Kuo, *Water Res.*, 1992, **26**, 881–886.
3 H. Zhang, M. Jiang, Z. Wang and F. Wu, *Color. Technol.*, 2007, **123**, 203–208.
4 K. S. Suslick, *Sci. Am.*, 1989, **260**, 80–86.
5 M. Pera Titus, V. Garcia Molina, M. A. Banos, J. Gimenez and S. Esplugas, *Appl. Catal., B*, 2004, **47**, 219–256.
6 J. Madhavan, P. S. S. Kumar, S. Anandan, F. Grieser and M. Ashokkumar, *J. Hazard. Mater.*, 2010, **177**, 944–949.
7 M. J. Allen, V. C. Tung and R. B. Kaner, *Chem. Rev.*, 2009, **110**, 132–145.
8 D. Li, M. B. Mueller, S. Gilje, R. B. Kaner and G. G. Wallace, *Nat. Nanotechnol.*, 2008, **3**, 101–105.
9 H. Sun, L. Cao and L. Lu, *Nano Res.*, 2011, **4**, 550–562.
10 S. Suresh, A. Pandikumar, S. Murugesan, R. Ramaraj and S. Paul Raj, *Mater. Express*, 2011, **1**, 307–314.
11 D. Pradhan, S. K. Mohapatra, S. Tymen, M. Misra and K. T. Leung, *Mater. Express*, 2011, **1**, 59–67.
12 M. Pal, J. Garcia Serrano, P. Santiago and U. Pal, *J. Phys. Chem. C*, 2007, **111**, 96–102.
13 Q. Xiang and J. Yu, *J. Phys. Chem. Lett.*, 2013, **4**, 753–759.
14 J. Guo, S. Zhu, Z. Chen, Y. Li, Z. Yu, Q. Liu, J. Li, C. Feng and D. Zhang, *Ultrason. Sonochem.*, 2011, **18**, 1082–1090.
15 R. Shi, Y. Wang, D. Li, J. Xu and Y. Zhu, *Appl. Catal., B*, 2010, **100**, 173–178.
16 E. Cavalli, A. Belletti and M. Brik, *J. Phys. Chem. Solids*, 2008, **69**, 29–34.
17 D. He, X. Zhang, T. Xie, J. Zhai, H. Li, L. Chen, L. Peng, Y. Zhang and T. Jiang, *Appl. Surf. Sci.*, 2011, **257**, 2327–2331.
18 G. B. Kumar, K. Sivaiah and S. Buddhudu, *Ceram. Int.*, 2010, **36**, 199–202.
19 F. Yang, C. Tu, H. Wang, Y. Wei, Z. You, G. Jia, J. Li, Z. Zhu, X. Lu and Y. Wang, *J. Alloys Compd.*, 2008, **455**, 269–273.
20 C. Yu and C. Y. Jimmy, *Mater. Sci. Eng., B*, 2009, **164**, 16–22.
21 A. Kalinko and A. Kuzmin, *J. Non-Cryst. Solids*, 2011, **357**, 2595–2599.
22 M. Sun, Y. Fang, Y. Wang, S. Sun, J. He and Z. Yan, *J. Alloys Compd.*, 2015, **650**, 520–527.
23 J. W. Xu, Z. D. Gao, K. Han, Y. Liu and Y. Y. Song, *ACS Appl. Mater. Interfaces*, 2014, **6**, 15122–15131.
24 W. S. Hummers Jr and R. E. Offeman, *J. Am. Chem. Soc.*, 1958, **80**, 1339.
25 M. M. J. Sadiq and A. S. Nesaraj, *J. Nanostruct. Chem.*, 2014, **5**, 45–54.
26 J. Qiu, C. Lai, Y. Wang, S. Li and S. Zhang, *Chem. Eng. J.*, 2014, **256**, 247–254.
27 Z. Liu, J. Y. Lee, W. Chen, M. Han and L. M. Gan, *Langmuir*, 2004, **20**, 181–187.
28 J. Xu, M. Chen and Z. Wang, *Dalton Trans.*, 2014, **43**, 3537–3544.
29 F. Zhang, F. Xiao, Z. H. Dong and W. Shi, *Electrochim. Acta*, 2013, **114**, 125–132.
30 S. Zhu, Y. Dong, X. Xia, X. Liu and H. Li, *RSC Adv.*, 2016, **6**, 23809–23815.
31 T. V. Nguyen, K. J. Kim and O. B. Yang, *J. Photochem. Photobiol., A*, 2005, **173**, 56–63.
32 P. Li, X. Zhao, C. J. Jia, H. Sun, L. Sun, X. Cheng, L. Liu and W. Fan, *J. Mater. Chem. A*, 2013, **1**, 3421–3429.
33 T. Yang, C. Shen, Z. Li, H. Zhang, C. Xiao, S. Chen, Z. Xu, D. Shi, J. Li and H. Gao, *J. Phys. Chem. B*, 2005, **109**, 23233–23236.
34 K. Garadkar, L. Ghule, K. Sapnar and S. Dhole, *Mater. Res. Bull.*, 2013, **48**, 1105–1109.
35 M. Hojamberdiev, G. Zhu and Y. Xu, *Mater. Res. Bull.*, 2010, **45**, 1934–1940.
36 A. Kumar, C. Guo, G. Sharma, D. Pathania, M. Naushad, S. Kalia and P. Dhiman, *RSC Adv.*, 2016, **6**, 13251–13263.
37 Y. Wang, Z. Wang, S. Muhammad and J. He, *CrystEngComm*, 2012, **14**, 5065–5070.
38 W. K. Jo and N. C. Selvam, *Dalton Trans.*, 2015, **44**, 16024–16035.
39 G. Williams and P. V. Kamat, *Langmuir*, 2009, **25**, 13869–13873.
40 L. Wang, J. Ding, Y. Chai, Q. Liu, J. Ren, X. Liu and W. L. Dai, *Dalton Trans.*, 2015, **44**, 11223–11234.
41 R. G. Pearson, *Inorg. Chem.*, 1988, **27**, 734–740.